

A modular supervised algorithm for vessel segmentation in red-free retinal images[☆]

Andrea Anzalone, Federico Bizzarri, Mauro Parodi, Marco Storace*

Biophysical and Electronic Engineering Department, University of Genoa, Via Opera Pia 11a, I-16145 Genova, Italy

Received 6 July 2007; accepted 24 May 2008

Abstract

In this paper, a supervised algorithm for vessel segmentation in red-free images of the human retina is proposed. The algorithm is modular and made up of two fundamental blocks. The optimal values of two algorithm parameters are found out by maximizing proper measures of performances (MOPs) able to evaluate from a quantitative point of view the results provided by the proposed algorithm. The choice of the MOP allows one to tailor the solution to the specific image features to be emphasized. The performances of the algorithm are compared with those of other methods described in the literature. The simulation results show a good trade-off between quality and processing speed times. For instance, in terms of the maximum average accuracy (MAA), K value, and specificity (SP), the best performance outcomes are 0.9587, 0.8069 and 0.9477, respectively.

© 2008 Elsevier Ltd. All rights reserved.

Keywords: Optimization; Blood vessel segmentation; Retinal vasculature mapping; Supervised algorithm; Retinal imaging

1. Introduction

Fundus photography (also known as “retinal photography”) refers to a non-invasive technique for the documentation of the posterior pole of the eye (retina and choroid). The evaluation of the vessels’ features in fundus images plays an important role in many medical diagnoses [2–4]. It can also be useful as a preliminary step for the registration of images of the same patient acquired at different times.

Vessel extraction can be performed by resorting to different methods (see [3,5] for an overview), either rule-based or supervised. In the latter case, the rule for vessel extraction is “learned” by the algorithm on the basis of a training set of manually processed reference images. Several algorithms based on supervised strategies have been recently proposed in the literature (see, for instance, [6–8]).

In this paper, we propose a modular supervised algorithm for the segmentation of retinal blood vessels in $M \times N$ -pixel

red-free images.¹ The algorithm performs two main operations, i.e., vessel enhancement and image binarization (plus cleaning), and it has two main characteristics:

- flexibility, thanks to its supervised nature and
- modularity.

Usually, all the parameters of algorithms for image processing are heuristically fixed a priori. In other cases, some parameters are fixed by using optimization procedures [9]. In this paper, we determine two “optimal” significant parameters by properly maximizing some measures of performances (MOPs) for the algorithm applied to a training set. Vessel enhancement involves the use of scale-space theory [11,12], and the most critical parameter in this part of the algorithm is the scale factor. The image binarization is based on a simple thresholding procedure, and the most critical parameter in this part of the algorithm is the threshold.

[☆] This work was supported by the MIUR, within the PRIN framework (Project no. 2004092944_003), and by the University of Genoa.

* Corresponding author. Tel.: +390103532079.

E-mail address: marco.storace@unige.it (M. Storace).

¹ “Red-free” images are obtained by extracting (*a posteriori*) from the original colour images the green channel, which gives the highest contrast between vessels and background [1].

Generally speaking, the algorithm subblocks are not new. The main novelty elements of this paper are:

- the use of optimization procedures (supervised, being applied to an image database with reference images) to determine two “optimal” parameters (scale factor and threshold);
- the combination of the subblocks to produce an accurate result as a trade-off between processing quality and computation complexity.

The obtained results are compared with those of other methods proposed in the literature.

The paper is organized as follows. The algorithm is briefly presented in Section 2, and the used MOPs are summarized in Section 3. The target function that is used to determine the optimal parameter values is defined in Section 4. In Section 5, some results are presented and the algorithm performances are discussed. Some concluding remarks are drawn in Section 6.

2. The algorithm

The algorithm is made up of two fundamental blocks (see the dashed boxes in Fig. 1, exhibiting in turn a modular structure. The grey elements are related to the supervised training algorithm that determines *a priori* the “optimal” parameters σ and n_{Th} . Once these parameters are fixed, the processing algorithm reduces to the black part of the scheme.

The first block performs a preliminary contrast enhancement (to compensate for the different illumination conditions of fundus images) and is devoted to vessel enhancement, while the second block provides a binary image by resorting to both a thresholding procedure and some cleaning operations.

Of course, each block may be replaced by other (modular) algorithms. For instance, for the first block one can resort to a multi-scale method for retinal image contrast enhancement based on the Contourlet transform [14] or to an algorithm for luminosity and contrast normalization [15].

The red-free image to be processed is viewed as a two-dimensional function $I(x, y)$ defined on a rectangular domain $\Omega \in \mathbb{R}^2$. The origin of the axes (x, y) is set in the centre of Ω . The function $I(x, y)$ represents a spatial distribution of grey levels, i.e., a surface of grey level intensities having a specific shape.

2.1. Contrast enhancement pre-processing

To compensate for the effects of a non-uniform lighting, common in this kind of images and due to changing

conditions during the acquisition process, a pre-processing of the images has to be carried out. Toward this end, we use the function ADAPTHISTEQ, contained in the Image Processing *Matlab*[®] Toolbox, which performs a contrast-limited adaptive histogram equalization (CLAHE) [16,17].

2.2. Vessel enhancement

To perform vessel enhancement, we adopt the method proposed in [18,19] and then used in [4] to process two-dimensional fundus images. The vessel enhancement procedure, devoted to highlighting geometric tube-like structures, is based on the Hessian operator H of the function $I(x, y)$, properly convoluted with a two-dimensional Gaussian function G with zero mean and standard deviation σ (see Eq. (1)) [11]:

$$G(x, y; \sigma) = \frac{1}{2\pi\sigma^2} e^{-(x^2+y^2)/2\sigma^2} \quad (1)$$

The convolution of I with G provides a low-pass filtering of I . This operation is useful since the evaluation of the second-order spatial derivatives of I increases the effects of the acquisition noise (which is certainly present in the image to be processed) and enhances high-frequency contents of the fundus image that are not useful for vessel segmentation.

According to scale-space theory,

$$H(I(x, y) \otimes G(x, y; \sigma)) = \begin{bmatrix} L_{xx}(x, y; \sigma) & L_{xy}(x, y; \sigma) \\ L_{yx}(x, y; \sigma) & L_{yy}(x, y; \sigma) \end{bmatrix} \quad (2)$$

where the symbol \otimes denotes convolution and

$$L_{\alpha\beta}(x, y; \sigma) = I(x, y) \otimes G_{\alpha\beta}(x, y; \sigma), \quad \alpha, \beta \in \{x, y\} \quad (3)$$

The eigenvalues λ_{\pm} of the Hessian H measure the convexity of the function $I \otimes G$ in the corresponding eigendirections [12]. At each point $(x, y; \sigma)$, the eigenvalue with the maximum absolute value is denoted by $\Lambda(x, y; \sigma)$ and the corresponding eigenvector is parallel to the direction of maximum curvature of the grey level. In the considered red-free images, a high positive curvature marks the presence of ridges in the low-pass filtered surface $I \otimes G$, i.e., the presence of vessels in the image. Then, the processed image can be obtained as follows:

$$\tilde{I}(x, y; \sigma) = \max(0, \Lambda(x, y; \sigma)) \quad (4)$$

The standard deviation σ is called *scale* and must be properly set. Basically, the scale fits the average vessel thickness

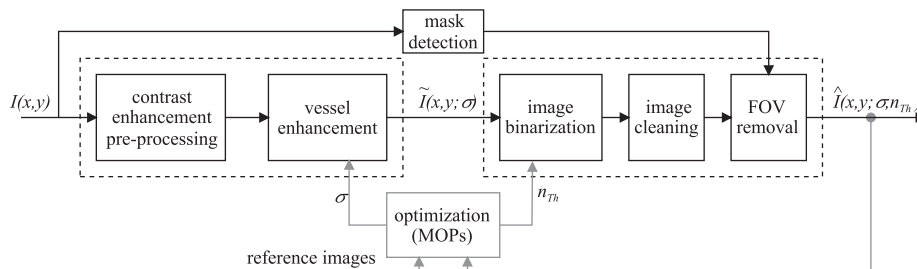


Fig. 1. Block scheme of the algorithm.

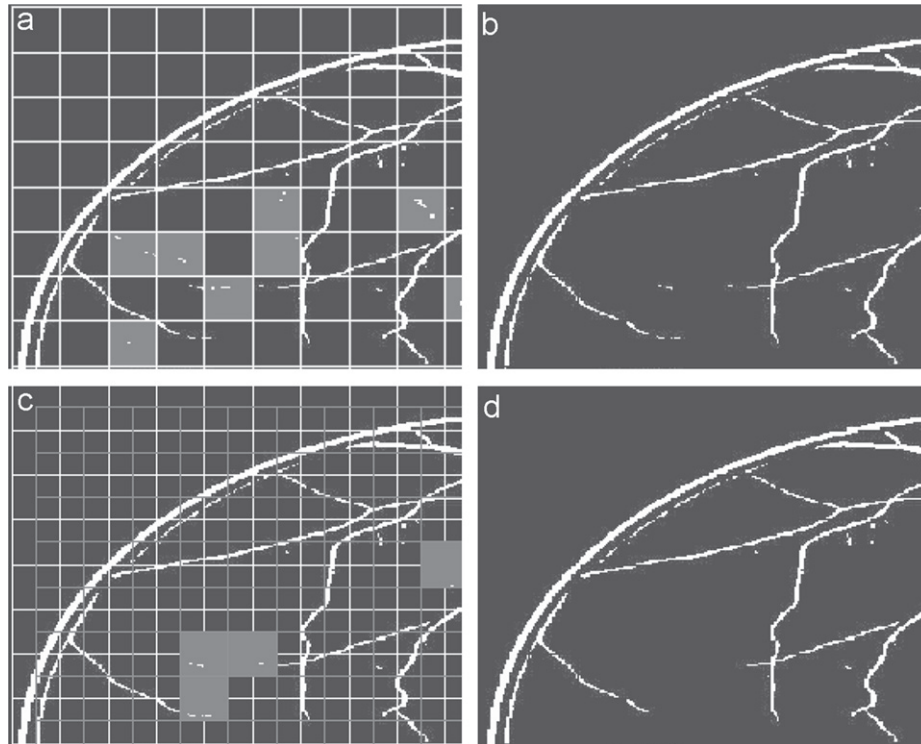


Fig. 2. An example of cleaning operation.

in each image considered. The multi-scale algorithms, for instance, process the image with different scales [4]. The results are usually accurate but at the cost of long computation times. In this paper, we set an “optimal” value for the parameter σ by properly maximizing some MOPs that are able to quantitatively measure the performances of the image processing algorithm.

Before performing the operations described in the next subsection, the histogram of the grey levels of $\tilde{I}(x, y; \sigma)$ is stretched between 0 and 255.

2.3. Image binarization and cleaning

In order to segment the vessels through image binarization, we must identify a proper threshold grey level Th . This threshold can be implicitly chosen by fixing the fraction n_{Th} of image pixels whose intensity levels will be set to 0, i.e., those pixels with grey levels between 0 and Th . By doing so, the value of Th turns out to be image dependent and is not affected by possible scalings of the image luminosity level. The value of n_{Th} will be directly derived by the optimization procedure described in Section 4.

Once the binary image is available, in some cases it can be desirable to delete spurious elements not belonging to the vessel network. Toward this end, we adopt a simple algorithm that, to the best of our knowledge, is original and illustrated in Fig. 2.

We fix a virtual grid made up of squares of $n \times n$ pixels and, for each square, we focus on the perimetric pixels. If all such pixels are black, we assume that the corresponding square contains either only background pixels or spurious elements

not connected to the vessel structure. In both cases, the whole square is set to black, thus removing the possible spurious elements. This cleaning algorithm can be iterated by changing n or the virtual grid position so as to accurately clean the image, but at the cost of an increasing computational effort. Fig. 2 shows what happens if we choose to iterate the algorithm only twice, with $n = 10$. In the first step, the grid completely covers the image (see a detail in Fig. 2(a)) and some spurious elements or not connected parts of vessels (see the grey squares in Fig. 2(a)) are removed, as shown in Fig. 2(b). In the second step, the grid is shifted by 5 pixels both horizontally and vertically (grey grid in Fig. 2(c)) and other elements (see the grey squares in Fig. 2(c)) are removed, as shown in Fig. 2(d).

As an alternative, thanks to the algorithm modularity, one may resort to other morphological solutions (e.g., area opening) for the cleaning block in order to achieve a different trade-off between speed and accuracy requirements.

Fig. 3 shows the normalized histogram of the green channel of a typical fundus image and the negative of a typical binary image obtained by resorting to the proposed vessel extraction algorithm, without doing any operation to remove the edge of the field of view (FOV). This edge is pointed out by the vessel enhancement block, and to remove it we must perform a proper set of operations. The histogram of the original image $I(x, y)$ (see Fig. 3(a)) exhibits an evident peak at very low grey levels. This peak is clearly distinct from the central part of the histogram, representing the FOV pixels. By resorting to a simple and robust thresholding operation, it is possible to define an $M \times N$ mask made up of white pixels corresponding to pixels of the FOV and to black pixels elsewhere.

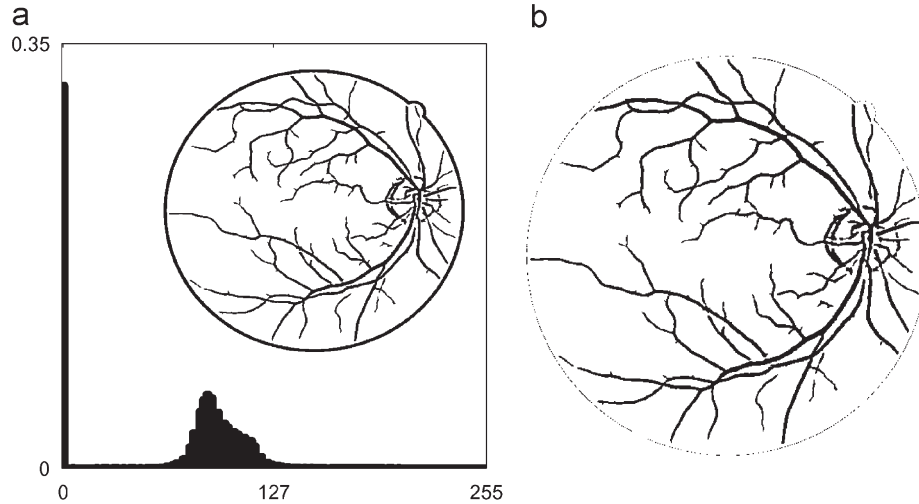


Fig. 3. (a) Histogram of a typical fundus image (green channel) and vessel tree with FOV and (b) negative of a typical binary image.

The logical multiplication of the binary image resulting from the vessel extraction algorithm with this mask provides images similar to the one shown in Fig. 3(b), where the edge of the FOV is not completely removed, due to lack of a preliminary erosion of the white portion of the mask. To accurately delete this edge, we can perform a slight erosion of the white portion of the mask by using, as structuring element, a disk of 5-pixel radius. This operation is not particularly sensitive, as only the peripheral portion of the vessel tree could be partially involved.

The image provided by the binarization, cleaning, and FOV removal blocks is called $\hat{I}(x, y; \sigma, n_{Th})$.

3. MOPs for vessel detection

Generally speaking, a MOP is nothing more than a quality measure that addresses how well a system works. In this section, some MOPs are introduced to evaluate, from a quantitative point of view, the results provided by the proposed algorithm.

The MOPs defined in the following are based on two images: a reference binary image \bar{I} —resulting from the manual segmentation of a fundus image I performed by people trained by an experienced ophthalmologist—and the binary image \hat{I} —resulting from the algorithm. The images I and \bar{I} used in this paper belong to the publicly available DRIVE database [3,13]. Some of the considered MOPs have been chosen to compare the performance outcomes with those of other algorithms tested on the same database.

We note that, since \hat{I} depends on the algorithm parameters σ and n_{Th} , also each MOP depends on σ and n_{Th} . For the sake of simplicity, however, in the next subsections such dependence will be omitted.

3.1. Maximum average accuracy (MAA)

The MAA evaluates the MOP of the vessel detection algorithm for the N_{FOV} pixels belonging to the FOV [20]. This

MOP expresses the number of pixels that have been correctly classified with respect to N_{FOV} :

$$MAA = 1 - \frac{\sum_{j,k \in FOV} |\bar{I}_{jk} - \hat{I}_{jk}|}{N_{FOV}} \in [0, 1] \quad (5)$$

3.2. K value

The K value is a measure of the agreement between two observers [21]:

$$K = \frac{OA - EA}{1 - EA} \in [-1, 1] \quad (6)$$

where OA is the *observed agreement* and EA is the *expected agreement*. The index OA expresses the percentage of pixels of \bar{I} that are correctly classified in \hat{I} , while the index EA expresses the probability that the two observations coincide. Indeed, EA can be interpreted as the algebraic sum of the product of the percentages of white pixels in \hat{I} and \bar{I} and the product of the percentages of black pixels in \hat{I} and \bar{I} .

3.3. Q value

This MOP is defined according to the universal image quality index considered in [22]. Such an index is “universal”, in the sense that the quality measure approach does not depend on the images being tested, the viewing conditions or the individual observers.

We consider two images, t and r , where t is the image whose quality must be evaluated (in our case, $t = \hat{I}$), whereas r is the reference image (in our case, $r = \bar{I}$). To define the index Q , we preliminarily introduce a square window $w(j, k)$ of $n_w \times n_w$ image pixels. Such a window slides over the images r and t , starting from the top-left corner and moving pixel by pixel horizontally and vertically through all the rows and columns of each image until the bottom-right corner is reached. The index

$Q \in [-1, 1]$ is defined as follows:

$$Q(t, r) = \frac{1}{|W|} \sum_{w(j,k) \in W} \frac{4\sigma_{tr}(j, k)\bar{t}(j, k)\bar{r}(j, k)}{(\sigma_t^2(j, k) + \sigma_r^2(j, k))(\bar{t}^2(j, k) + \bar{r}^2(j, k))} \quad (7)$$

where $|W|$ is the overall number of possible different positions of the window w over each image, and $\bar{t}(j, k)$ and $\bar{r}(j, k)$, $\sigma_t^2(j, k)$ and $\sigma_r^2(j, k)$, and $\sigma_{tr}(j, k)$ are the mean values, the variances, and the covariances, respectively, of the images t and r at each window position. The explicit expressions used to calculate the mean values, the variances and the covariances of the images t and r at each window position are provided in Appendix A. For the Q value, we set $n_w = 8$ to have a window large enough to obtain reliable estimates of the mean, variance and covariance of this MOP.

3.4. Sensitivity and specificity

Sensitivity (SN) (i.e., the ability to detect vessel pixels) and specificity (SP) (i.e., the ability to detect non-vessel pixels) are good indicators for showing the utility of an algorithm in particular in the medical applications framework. These two measures can be combined to define a MOP whose maximization aims to obtain the algorithm parameters balancing these two important quality indices. In particular this MOP can be defined as follows:

$$\text{SNSP} = -(\text{SN} \times \text{SP} - 1)^2 \in [-1, 0] \quad (8)$$

where SP is defined as the ratio between the number of true positive pixels and the number of positive instances and SN is given by the ratio between the number of true negative pixels and the number of negative instances. This MOP assumes its maximum value if both SP and SN are equal to 1, i.e., the algorithm exhibits the best capability to distinguish between vessel and non-vessel pixels.

4. Optimization

The binary images obtained by resorting to the supervised algorithm proposed in this paper depend on the algorithm parameters σ and n_{Th} . Therefore, it is necessary to define a procedure to choose proper values for these parameters in order to ensure a good quality of the results. Toward this end, a training set made up of N_{TS} fundus images (together with their reference segmentations) can be used, and σ and n_{Th} can be fixed by maximizing the quality of the results obtained by processing the images belonging to it. In this respect, the proposed algorithm turns out to be supervised. From a practical point of view, one can choose one of the MOPs introduced in the previous section, and then either maximize the following target function

$$F(\sigma, n_{\text{Th}}) = \frac{1}{N_{\text{TS}}} \sum_{k=1}^{N_{\text{TS}}} \text{MOP}_k(\sigma, n_{\text{Th}}) \quad (9)$$

or minimize $-F(\sigma, n_{\text{Th}})$.

Table 1

Values of σ , n_{Th} , best and worst cases after optimization, for each MOP

MOP	σ	n_{Th}	Best case	Worst case
MAA	2.0253	0.90946	0.9541	0.9067
K	2.1505	0.89261	0.7610	0.5958
Q	2.0882	0.88603	0.7295	0.5406
SNSP	2.7427	0.8267	-0.3086 (SN = 0.4712 SP = 0.9433)	-0.3737 (SN = 0.4189 SP = 0.9278)

In our optimizations, we used the simplex search method [23] implemented in the *fminsearch Matlab*[®] function to minimize $-F(\sigma, n_{\text{Th}})$. The ranges considered for the optimization parameters were: $\sigma^2 \in [1, 8]$ and $n_{\text{Th}} \in [0.8, 0.95]$. In this domain, the target function $-F$ was convex for all the MOPs considered, then a local optimization algorithm was sufficient.

5. Results

To derive the image-processing results reported in this section as benchmarks for the proposed algorithm, the 40 fundus images making up the DRIVE database and their “gold” standard manual segmentation [3,13] were used. In particular, our training set contained the last 20 images ($N_{\text{TS}} = 20$) of the database, whereas the first 20 images were a test set used to measure the performances of the algorithm whose parameters had been tuned according to the optimization procedure.

The cleaning operation was iterated for many values of n . For each value of n , the corresponding grid was shifted in the image by positioning its upper-left vertex in all the pixels (j, k) for $j = 1, \dots, n - 1$ and $k = 1, \dots, n - 1$. The sequence of values assigned to n was $\{3, 4, 8, 16, 4, 8, 16\}$ and was chosen heuristically after many trials. We needed to repeat twice some values of n in the sequence, since a single application would have cleaned only one element of pairs of close spurious patterns.

5.1. Training phase

During the training phase, for each MOP defined in the previous section, the optimal values of the algorithm parameters σ and n_{Th} were obtained by maximizing $F(\sigma, n_{\text{Th}})$. These values are given in the first and second columns of Table 1, respectively. The MOPs values corresponding to the best and worst cases are shown in the third and fourth columns, respectively. These values were obtained by processing the images of the training set with the optimal values of the algorithm parameters. The SN values provided by the algorithm are lower than some others reported in the literature (see, for instance, [24]) since our algorithm is simpler in order to privilege its modular structure and its processing speed. By increasing either the numbers of the elementary building blocks or their complexity the SN values might be increased too. Fig. 4 shows the corresponding image-processing results, i.e., the best (first row) and worst (second row) vessel extraction results for the training

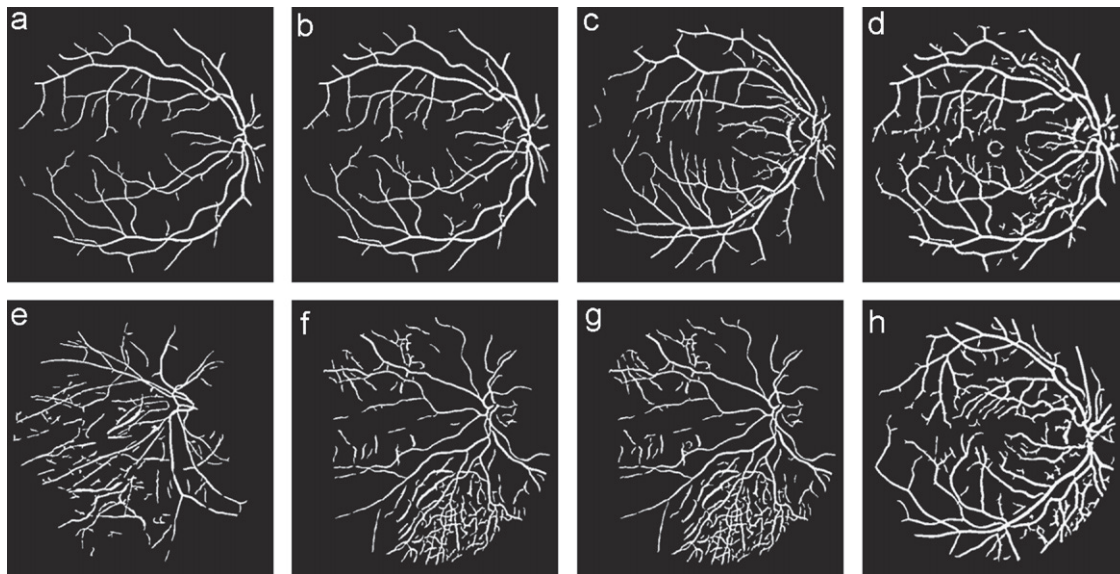


Fig. 4. Image-processing results for the training set.

Table 2

Mean values, standard deviations, best and worst cases, mean TPF and FPF for the MOPs with σ and n_{Th} set to their optimal values

MOP	Mean	Standard deviation	Best case	Worst case	Mean TPF	Mean FPF
MAA	0.94183	0.00822	0.9587	0.9275	0.6377	0.0091
K	0.72860	0.03452	0.8069	0.6642	0.7052	0.0162
Q	0.69123	0.03933	0.7735	0.6247	0.7246	0.0193
SNSP	−0.32751	0.01214	−0.3055 (SN = 0.4720 SP = 0.9477)	−0.3468 (SN = 0.4384 SP = 0.9376)	0.8260	0.0570

set images in terms of MAA (a,e), K (b,f), Q (c,g), and SNSP (d,h). The number of original images in the database is also given. It is quite evident that the results obtained by using SNSP, due to the higher value of the corresponding optimal σ , are characterized by larger vessel trees.

Once the optimal values of σ and n_{Th} have been obtained, the algorithm can be applied to other images to test its performances.

5.2. Test phase

The first two columns of Table 2 contain the mean values and the standard deviations, respectively, of the MOPs obtained by processing the images of the test set after fixing the parameters σ and n_{Th} at their optimal values (see Table 1). The values of the MOPs corresponding to the best (third column) and worst (fourth column) cases are also shown. The fifth and sixth columns contain the mean values of the True Positive Fraction (for each image, the percentage of vessel pixels actually classified as vessel pixels) or TPF and of the False Positive Fraction (for each image, the percentage of non-vessel pixels actually classified as vessel pixels) or FPF, respectively, for the 20 images of the test set. In Fig. 5, the segmented images corresponding to the best (first row) and worst (second row) cases are provided for the test set in terms of MAA (a,e), K (b,f), Q

(c,g), and SNSP (d,h). The number of original images in the database is given.

5.3. Comparisons with other methods

By resorting to the first two MOPs (MAA and K), it is possible to compare the performances of the proposed algorithm with the ones of other algorithms that can be found in the literature. The first two columns of Table 3 contain the mean values of both MAA and K , obtained by a second independent manual segmentation available for the first 20 images of the DRIVE database (first row) and by processing the test set images according to different methods [3,20]: primitive-based method [3], pixel classification method [20], mathematical morphology and curve estimation method [25], verification-based local thresholding method [26], scale-space analysis and region growing approach [27], and matched filter method [28]. Among these algorithms, only the pixel classification and primitive-based methods are supervised.

The last two columns of Table 3 contain the mean values of TPF and FPF, respectively, for some of the methods considered. In particular, for our method, we have provided the mean TPF and FPF for Q , which yields the best results (see Table 2). Actually, on average, SNSP yields the best TPF, but also the worst FPF.

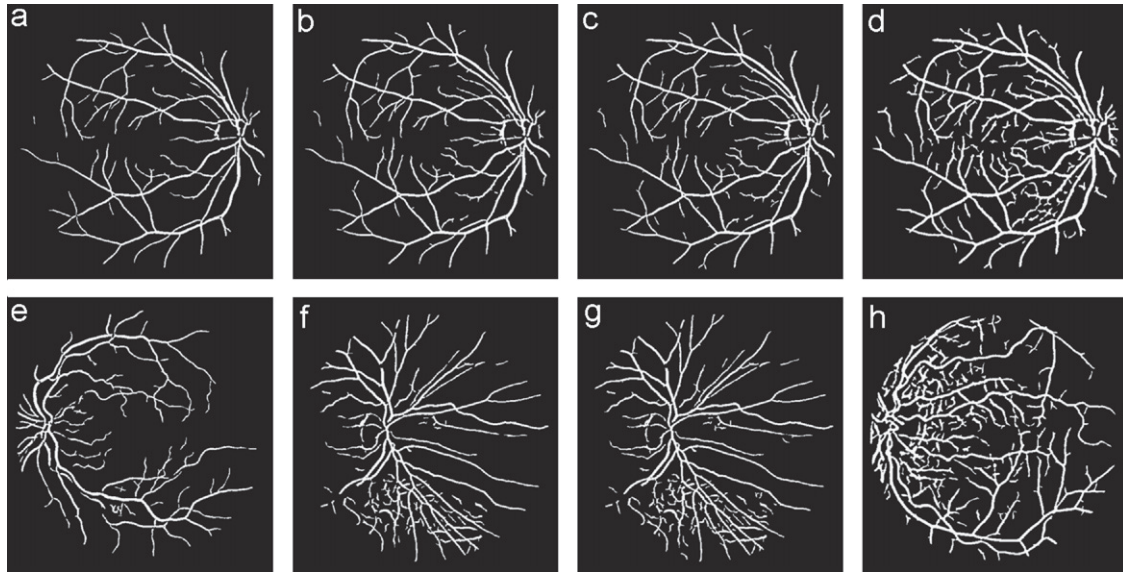


Fig. 5. Image-processing results for the test set.

Table 3
Comparisons with other methods proposed in the literature

Method	MAA	K	TPF	FPF
Second manual segmentation	0.9473	0.7589	0.776	0.0275
Primitive-based method	0.9441	0.7345	0.697	0.019
Our algorithm	0.9419	0.7286	0.7246	0.019
Pixel classification	0.9416	0.7145		
Mathematical morphology and curve estimation	0.9377	0.6971		
Verification-based local thresholding	0.9212	0.6399		
Scale-space analysis and region growing	0.9181	0.6389	0.7246	0.0345
Matched filter	0.8773	0.3357		
All background	0.8727	0		

Comparisons of the results summarized in Tables 2 and 3 point out that the performances of the proposed algorithm are close to the ones of well-known algorithms presented in the literature. In particular, we obtain a mean value of 0.9419 for the MAA and a mean value of 0.7286 for the agreement between two observers (K -value). On the whole, the results confirm that supervised methods represent a reliable way to get the best results. We remark that, for our case, the algorithm is much less computationally expensive than the best algorithm in Table 3. Using a Matlab[®] implementation and not a faster C++ one, running on an Intel[®] Celeron[®] CPU 2.40GHz with 192Mb RAM, the initial optimization phase of our algorithm can take several minutes but, once the “optimal” values for parameters σ and n_{Th} have been fixed, each segmentation of a fundus image does not require more than six seconds, for images of 564×584 pixels. The primitive-based method algorithm, instead, requires a processing time of several minutes, under similar conditions [3]. We remark that the modular structure of the proposed algorithm may allow a further speed-up of the computations if combined with a pipeline architecture, i.e., if the subblocks can process different images in parallel.

5.4. MOPs influence on the results

By using the Q value as a MOP, we show how different features of the results can be highlighted. In particular, with this MOP we can detect a larger number of small vessels, related to higher values of the mean TPF for this MOP (see Table 2). The cost involved is a larger number of wrongly classified pixels, related to higher values of the mean FPF (see Table 2). Anyway, we remark that these new false positives are confined to regions close to image elements denoting the presence of some pathologies (e.g., drusen, exudates, age-related macular degeneration) and then they affect the results only for images containing this kind of elements. For instance, Fig. 6 shows

- vessel segmentation of an image with no pathologies, for σ and n_{Th} obtained by training with (a) MAA and (b) Q ;
- vessel segmentation of an image with signs of mild early diabetic retinopathy, for σ and n_{Th} from the training with MAA (c) and with Q (d).

The number of original images in the database is given.

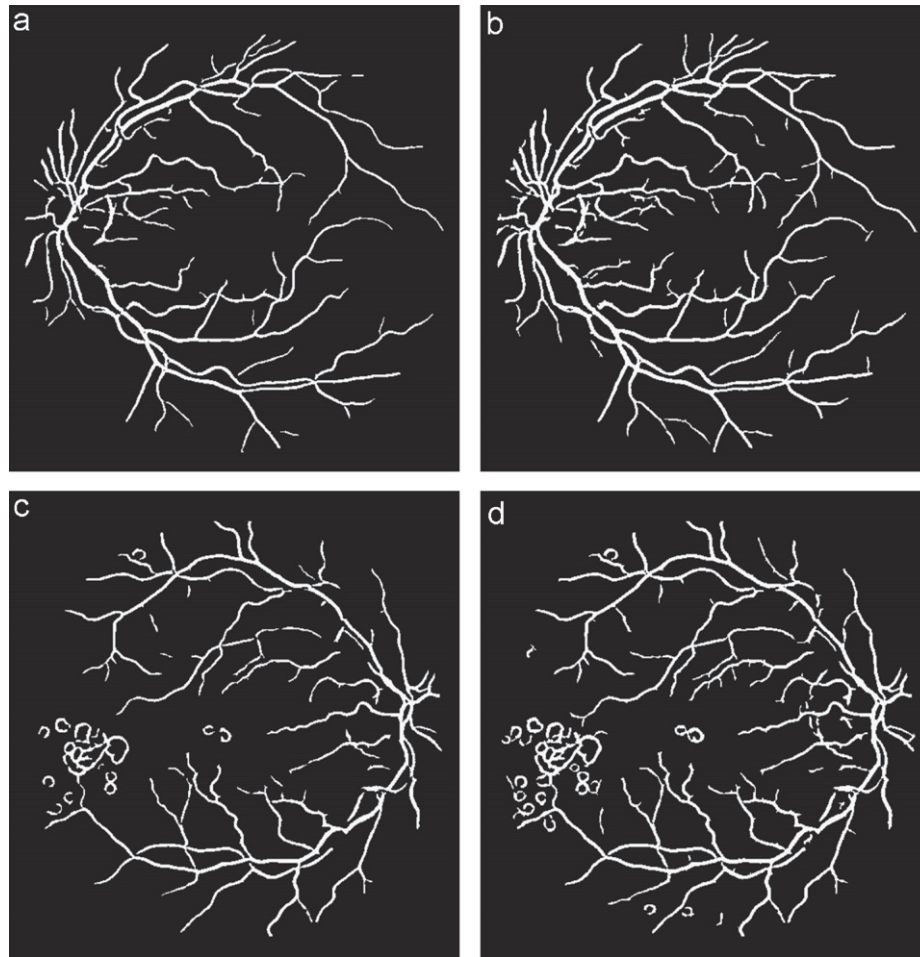


Fig. 6. Vessel segmentation of different kinds of images (see text).

The same effects can be observed, even more emphasized, by using the SNSP value as a MOP.

6. Discussion and conclusions

A supervised algorithm for vessel segmentation in red-free images of the human retina has been proposed. The choice of two algorithm parameters seems to be particularly critical. The “optimal” values for these parameters can be obtained by optimizing proper target functions, defined on the basis of some MOPs. In principle, different MOPs can be chosen to highlight different features in the processed images to meet specific requirements. We have referred in particular to four examples of MOPs. We point out that nowadays there is, in the literature, no common opinion about a universal MOP able to evaluate adequately the results of most of algorithms. Moreover, different applications may need different degrees of attention on specific aspects of the results; as examples, one may be interested in obtaining a higher accuracy of small vessels or in determining the vessels’ widths or in finding at best the ramifications of the vessels’ tree. Several applications do not require all the cited features nor that all these features be detected at the same time. The proposed algorithm is flexible enough to

be adapted to different applications, simply by changing the reference MOP.

We have experimentally verified that choosing the threshold Th implicitly, by fixing the fraction n_{Th} of image pixels whose intensity level is set to 0, provides better results than choosing Th directly. For instance, in the latter case, we obtain a mean value of 0.94015 and a standard deviation of 0.00898 for MAA, which is a worse result as compared with the first row in Table 2.

With respect to other Hessian-based methods (e.g., [4]), where two or more thresholds are required, our choice of defining the algorithm only for red-free images (setting to zero the eigenvalue $\lambda(x, y)$ with maximum absolute value for negative curvature regions) allowed us to obtain satisfactory results with only one threshold. Indeed, in this case, the only high-curvature structures are the vessels. We point out that the same algorithm is valid for the negatives of fluorescein images.

The choice of a single “optimal” scale factor σ , instead of a multi-scale approach, yields similar results and considerably reduces the computational effort. As a matter of fact, by using the 20 images of the test set, by a multi-scale algorithm we obtained the best average MAA = 0.9423, with scales within the interval of $1 \leq s \leq 10$ pixels in steps of 1 pixel and with

optimization only on n_{Th} . With our algorithm, the best average MAA was 0.94183 (see Table 2). A further visual inspection of the results points out that there are no appreciable differences in the detection of small vessels. Only slight differences in the widths of vessels can be noticed.

We have already remarked that the cleaning procedure deletes all the spurious elements. It may happen that some of these spurious elements belong to thin vessels, which remain therefore unconnected to the main tree. Specific measures allowed us to state that this is a marginal behaviour. As compared with the complete algorithm, a version not containing the cleaning procedure causes an increase of 30% in the FPF and of only 4% in the TPF. This confirms that most of unconnected spurious little clusters do not belong to the vessel tree. These measures are average values for the 20 images of the test set and have been obtained by σ and n_{Th} fixed after the training with MAA (see Table 1).

The modular structure of the algorithm, allows one to look for the desired compromise between quality and complexity. As a matter of fact, the two main processing blocks are, in turn, made up of subblocks, thus making the algorithm highly modular, with the possibility of applying only a subset of the possible processing operations. Most of the subblocks, moreover, can be implemented by enhancing either the processing accuracy or the simplicity. In the latter case, one reduces complexity and computation times at the cost of lower quality of results [10].

Finally, we remark that the quality of the results may be further improved by adding other processing blocks. For instance, a procedure for removing pixels belonging to the edge of the optic disk could be introduced. Another improvement for images showing some pathology (e.g., drusen, exudates, and others) may be obtained by a block for the elimination of light objects before segmenting the vessels in pathological images. As a matter of fact, Fig. 6 points out that light objects in pathological images usually have a bad influence on results, mainly when the objects are near or touch the vascular network. The presence of a block that eliminates these objects before vessel segmentation should overcome this drawback, thus having a positive influence on the calculation of σ and n_{Th} .

Conflict of interest statement

None declared.

Acknowledgements

The authors wish to thank Dr. Federico Ricci (Department of Biopathology, University of Rome “Tor Vergata”) and Prof. Carlo Enrico Traverso (Dipartimento di Scienze Neurologiche, Oftalmologia e Genetica, University of Genoa) for stimulating comments and discussions.

Appendix A.

Explicit expressions used to calculate the mean values, the variances and the covariances of the images t and r at each

window position:

$$\bar{t}(j, k) = \frac{1}{n_w^2} \sum_{p, q \in w(j, k)} t(p, q) \quad (A.1)$$

$$\sigma_t^2(j, k) = \frac{1}{n_w^2 - 1} \sum_{p, q \in w(j, k)} (t(p, q) - \bar{t}(j, k))^2 \quad (A.2)$$

$$\sigma_{tr} = \frac{1}{n_w^2 - 1} \times \sum_{p, q \in w(j, k)} (t(p, q) - \bar{t}(j, k))(r(p, q) - \bar{r}(j, k)) \quad (A.3)$$

Eqs. (A.1) and (A.2) apply, *mutatis mutandis*, also to r .

References

- [1] A. Hoover, V. Kouznetsova, M. Goldbaum, Locating blood vessels in retina images by piecewise threshold probing of matched filter response, *IEEE Trans. Med. Imag.* 19 (2000) 203–210.
- [2] C. Tsai, C. Stewart, H. Tanebaum, B. Roysam, Model-based method for improving the accuracy and repeatability of estimating vascular bifurcation and crossovers from retinal fundus images, *IEEE Trans. Inf. Technol. Biomed.* 8 (2004) 122–130.
- [3] J. Staal, M. Abramoff, M. Niemeijer, M. Viergever, B. van Ginneken, Ridge-based vessel segmentation in color images of the retina, *IEEE Trans. Med. Imag.* 23 (2004) 501–509.
- [4] M. Martinez-Perez, A. Hughes, S. Thom, A. Bharath, K. Parker, Segmentation of blood vessels from red-free and fluorescein retinal images, *Med. Image Anal.* 11 (2007) 47–61.
- [5] C. Kirbas, F. Quek, A review of vessel extraction techniques and algorithms, *ACM Comput. Surv.* 36 (2004) 81–121.
- [6] S. Salem, N. Salem, A. Nandi, Segmentation of retinal blood vessels using a novel clustering algorithm (RACAL) with a partial supervision strategy, *Med. Biol. Eng. Comput.* 45 (2007) 261–273.
- [7] J.V.B. Soares, J.J.G. Leandro, R.M. Cesar, H.F. Jelinek, M.J. Cree, Retinal vessel segmentation using the 2-D Gabor wavelet and supervised classification, *IEEE Trans. Med. Imag.* 25 (2006) 1214–1222.
- [8] E. Ricci, R. Perfetti, Retinal blood vessel segmentation using line operators and support vector classification, *IEEE Trans. Med. Imag.* 26 (2007) 1357–1365.
- [9] M. Al-Rawi, M. Qutaishat, M. Arrar, An improved matched filter for blood vessel detection of digital retinal images, *Comput. Biol. Med.* 37 (2007) 262–267.
- [10] A. Anzalone, F. Bizzarri, P. Camera, L. Petrillo, M. Storace, DSP implementation of a low-complexity algorithm for real-time automated vessel detection in images of the fundus of the human retina, in: *Proceedings of the 2007 IEEE International Symposium on Circuits and Systems (ISCAS'2007)*, May 27–30, 2007, pp. 97–100.
- [11] T. Lindeberg, *Scale-Space Theory in Computer Vision*, Kluwer Academic Publishers, The Netherlands, 1994.
- [12] D. Eberly, *Ridges in Image and Data Analysis (Computational Imaging and Vision)*, Springer, Berlin, 1996.
- [13] (<http://www.isi.uu.nl/Research/Databases/DRIVE/>).
- [14] P. Feng, Y. Pan, B. Wei, W. Jin, D. Mi, Enhancing retinal image by the Contourlet transform, *Pattern Recognition Lett.* 28 (2007) 516–522.
- [15] M. Foracchia, E. Grisan, A. Ruggeri, Luminosity and contrast normalization in retinal images, *Med. Image Anal.* 9 (2005) 179–190.
- [16] S. Pizer, E. Amburn, J. Austin, R. Cromartie, A. Geselowitz, T. Greer, B. ter Haar Romeny, J. Zimmerman, K. Zuiderveld, Adaptive histogram equalization and its variations, *Comput. Vision Graphics Image Process.* 39 (1987) 355–368.
- [17] K. Zuiderveld, Contrast limited adaptive histogram equalization, in: *Graphics Gems IV*, Academic Press, San Diego, CA, USA, 1994, pp. 474–485.

- [18] Y. Sato, S. Nakajima, H. Atsumi, T. Koller, G. Gering, S. Yoshida, R. Kikinis, 3D multi-scale line filter for segmentation and visualization of curvilinear structures in medical images, in: Proceedings of the CVRMed-MRCAS, 1997, pp. 213–222.
- [19] C. Lorenz, I. Carlsen, T. Buzung, C. Fassnacht, J. Weese, Multi-scale line segmentation with automatic estimation of width, contrast and tangential direction in 2D and 3D medical images, in: Proceedings of the CVRMed-MRCAS, 1997, pp. 233–242.
- [20] M. Niemeijer, J. Staal, B. van Ginneken, M. Loog, M. Abramoff, Comparative study of retinal vessel segmentation methods on a new publicly available database, in: Proceedings of the SPIE Medical Imaging 2004, May 2004, pp. 648–656.
- [21] J. Landis, G. Koch, The measurement of observer agreement for categorical data, *Biometrics* 33 (1977) 159–174.
- [22] Z. Wang, A. Bovik, A universal image quality index, *IEEE Signal Process. Lett.* 9 (2002) 81–84.
- [23] J.C. Lagarias, J.A. Reeds, M.H. Wright, P.E. Wright, Convergence properties of the Nelder–Mead simplex method in low dimensions, *SIAM J. Optim.* 9 (1998) 112–147.
- [24] D.A. Adjeroh, U. Kandaswamy, O.J. Vernon, Texton-based segmentation of retinal vessels, *JOSA A* 25 (2007) 1384–1393.
- [25] F. Zana, J. Klein, A multimodal registration algorithm of eye fundus images using vessels detection and hough transform, *IEEE Trans. Med. Imag.* 18 (1999) 419–428.
- [26] X. Jiang, D. Mojon, Adaptive local thresholding by verification-based multithresholding probing with application to vessel detection in retinal images, *IEEE Trans. Pattern Anal. Mach. Intell.* 25 (2003) 131–137.
- [27] M. Martinez-Perez, A. Hughes, A. Stanton, S. Thom, A. Bharath, K. Parker, Scale-space analysis for the characterisation of retinal blood vessels, in: Proceedings of the Image Understanding and Analysis (MIUA'99), July 1999, pp. 57–60.
- [28] S. Chaudhuri, S. Chatterjee, N. Katz, M. Nelson, M. Goldbaum, Detection of blood vessels in retinal images using two-dimensional matched filters, *IEEE Trans. Med. Imag.* 8 (1989) 263–269.

Federico Bizzarri was born in Genoa, Italy, in 1974. He received his “Laurea” (M.Sc.) five-year degree (*Summa Cum Laude*) in Electronic Engineering in October 1998 and his Ph.D. degree in Electrical Engineering on November 2001, both from the University of Genoa, Italy. His main research interests are in the area of nonlinear circuits, with emphasis on chaotic dynamics and bifurcation theory, circuit models of nonlinear systems, circuit theory, image processing.

Mauro Parodi was born in Genoa on November 11, 1948. He received the graduate degree in Electronic Engineering (*Summa Cum Laude*) from the University of Genoa, Genoa, Italy, in 1972. He joined the University of Genoa as an Assistant Professor in Electronic Computers, in 1973, and in 1982, became Associate Professor of Electrical Network Theory. Since 1985, he has been a Full Professor of Basic Circuit Theory at the Biophysical and Electronic Engineering Department of the University of Genoa. His research interests concern nonlinear circuits and systems, molecular electronics, electrical modelling of materials, circuit modelling of devices, image processing, optimization problems.

Marco Storace was born in Genoa, Italy, in 1969. He received the “Laurea” (M.Sc.) five-year degree (*Summa Cum Laude*) in Electronic Engineering in March 1994 and the Ph.D. degree in Electrical Engineering in April 1998, both from the University of Genoa, Italy. Since 2004 he has been an Associate Professor in the Department of Biophysical and Electronic Engineering, University of Genoa. He was a visitor to EPFL, Lausanne, Switzerland, in 1998 and 2002. His main research interests are in the area of nonlinear circuit theory and applications, with emphasis on circuit models of nonlinear systems (e.g., hysteresis, biological neurons), methods for the piecewise-linear approximation of nonlinear systems and for the consequent circuit synthesis, methods of analysis and synthesis of cellular circuits, variational methods for image processing, and nonlinear dynamics. He is the author or coauthor of about 70 scientific papers, more than an half of which have been published in international journals.

Andrea Anzalone was born in Genoa, Italy, in 1979. In 2004 he received his “Laurea” (M.Sc.) five-year degree (*Summa Cum Laude*) in Electronic Engineering from the University of Genoa, Italy, where he is currently a Ph.D. student in Electrical Engineering. His main research interests are in the area of image processing, with emphasis on: use of parallel architectures to solve variational problems in early vision applications, use of archives of images in problems of classification or segmentation, biomedical applications.